

TRIGONOMETRIC PARALLAXES OF MASSIVE STAR-FORMING REGIONS. IV. G35.20–0.74 AND G35.20–1.74

B. ZHANG^{1,2}, X. W. ZHENG¹, M. J. REID³, K. M. MENTEN⁴, Y. XU^{4,5}, L. MOSCADELLI⁶, AND A. BRUNTHALER⁴

¹ Department of Astronomy, Nanjing University, Nanjing 210093, China

² Shanghai Astronomical Observatory, Chinese Academy of Sciences, Shanghai 200030, China

³ Harvard-Smithsonian Center for Astrophysics, 60 Garden Street, Cambridge, MA 02138, USA

⁴ Max-Planck-Institut für Radioastronomie, Auf dem Hügel 69, 53121 Bonn, Germany

⁵ Purple Mountain Observatory, Chinese Academy of Sciences, Nanjing 210008, China

⁶ INAF, Osservatorio Astrofisico di Arcetri, Largo E. Fermi 5, 50125 Firenze, Italy

Received 2008 July 16; accepted 2008 October 29; published 2009 March 2

ABSTRACT

We report trigonometric parallaxes for the high-mass star-forming regions G35.20–0.74 and G35.20–1.74, corresponding to distances of $2.19^{+0.24}_{-0.20}$ kpc and $3.27^{+0.56}_{-0.42}$ kpc, respectively. The distances to both sources are close to their near kinematic distances and place them in the Carina–Sagittarius spiral arm. Combining the distances and proper motions with observed radial velocities gives the locations and full space motions of the star-forming regions. Assuming a standard model of the Galaxy, G35.20–0.74 and G35.20–1.74 have peculiar motions of $\approx 13 \text{ km s}^{-1}$ and $\approx 16 \text{ km s}^{-1}$ counter to Galactic rotation and $\approx 9 \text{ km s}^{-1}$ toward the North Galactic Pole.

Key words: astrometry – Galaxy: structure – stars: individual (G35.20–0.74, G35.20–1.74) – techniques: interferometric

1. INTRODUCTION

G35.20–0.74 (IRAS 18556+0136) and G35.20–1.74 (IRAS 18592+0108) are high-mass star-forming regions. They both are home to strong methanol (CH_3OH) masers at 12 GHz and were selected as targets for our large project with the NRAO⁷ Very Long Baseline Array (VLBA) to study the spiral structure and kinematics of the Milky Way. Details of this project are discussed in Reid et al. (2009a), hereafter called Paper I.

The kinematic distance of G35.20–0.74 is about 3.3 kpc, based a CO line velocity of 35 km s^{-1} (Solomon et al. 1987). This star-forming region is home to a massive protostar with a jet driven outflow, rarely observed toward massive young stellar objects. Sub-arcsecond resolution Very Large Array (VLA) observations of the region by Gibb et al. (2003) at 3.5 and 6.0 cm show that three concentrations of radio continuum emission break up into 11 individual sources all lying along the outflow. As for most high-mass star-forming regions, G35.20–0.74 contains water and OH masers (Forster & Caswell 1989), methanol masers (Caswell et al. 1995), and many thermal lines from molecules like CH_3CN (Kalenskii et al. 2000), HCO^+ and HCN (Gibb et al. 2003) have been detected. This region was also observed recently at mid-infrared wavelengths by De Buizer et al. (2006). These observations reveal an extended source with a cometary shape with the masers concentrated around the head.

The G35.20–1.74 star-forming region also contains water, OH and methanol masers, and a large cometary UCHII region. The UCHII region, known as W48A, lies about $20''$ from the water and OH masers. Mid-infrared images (De Buizer et al. 2004) show a bright point source at the location of the water masers as well as the UCHII region to the south-east. Kinematic distances to G35.20–1.74, from various molecular lines associated with W48A (Genzel & Downes 1977; Palagi

et al. 1993; Churwell et al. 1990; Braz & Epchtein 1983; Vallee & MacLeod 1990), range between 3.0 and 3.4 kpc.

Starting at the Sun, a ray toward Galactic longitude 35° first crosses the Carina–Sagittarius spiral arm, then the Crux–Scutum arm, before recrossing the Carina–Sagittarius arm and then crossing the Perseus arm. Thus distances are crucial to establish to which arm G35.20–0.74 and G35.20–1.74 belong. Given the large kinematic anomalies measured for some massive star-forming regions, for example for W3OH (Xu et al. 2006a; Hachisuka et al. 2006), it is important to measure distances to these and other sources by direct methods such as trigonometric parallax.

2. OBSERVATIONS AND CALIBRATION PROCEDURES

On 2005 October 30, 2006 April 7 and October 7, and 2007 April 16, we observed methanol masers at 12 GHz toward G35.20–0.74 and G35.20–1.74 with 8 hr tracks on the VLBA. Since, for these sources, the declination parallax signature is considerably smaller than for right ascension, we scheduled the observations so as to maximize the right ascension parallax offsets. We observed several extragalactic radio sources as background references which provide independent checks for parallax solutions. Table 1 lists the positions, intensities, source separations, observed radial velocities and beam sizes.

Our general observing setups and calibration procedures are described in Paper I, and here we discuss only aspects of the observations that are specific to G35.20–0.74 and G35.20–1.74. We observed two ICRF sources, J1800+3848 and J1800+7828 (Ma et al. 1998), near the beginning, middle, and end of the observations in order to monitor delay and electronic phase differences among the observing bands. The right and left-circularly polarized emission from the 12 GHz methanol masers toward G35.20–0.74 and G35.20–1.74 were observed in 4 MHz bands centered at Local Standard of Rest (LSR) velocities of 31 km s^{-1} and 43 km s^{-1} , respectively.

The strongest maser spots at V_{LSR} of 28.3 km s^{-1} and 41.5 km s^{-1} served as the phase-references for G35.20–0.74 and

⁷ The National Radio Astronomy Observatory is a facility of the National Science Foundation operated under cooperative agreement by Associated Universities, Inc.

Table 1
Positions and Brightnesses

Source	R.A. (J2000) (h m s)	Decl. (J2000) ($^{\circ}$ ' ")	T_b (Jy/b)	θ_{sep} ($^{\circ}$)	P.A. ($^{\circ}$)	V_{LSR} (km s $^{-1}$)	Beam (mas)
G35.20–0.74	18 58 13.0517	+01 40 35.674	0.7–0.9	31	1.2
J1855+0215	18 55 00.1130	+02 15 41.100	0.03	1.0	–54
J1855+0251	18 55 35.4365	+02 51 19.562	0.20	1.4	–29
J1907+0127	19 07 11.9963	+01 27 08.963	0.10	2.3	+96
G35.20–1.74	19 01 45.5364	+01 13 32.545	3.5–9.5	43	1.2
J1903+0145	19 03 53.0632	+01 45 26.306	0.18	0.8	+45
J1904+0110	19 04 26.3978	+01 10 36.696	0.33	0.7	+94
J1907+0127	19 07 11.9963	+01 27 08.963	0.30	1.4	+80
J1855+0251	18 55 35.4365	+02 51 19.562	0.50	2.2	–43

Notes. The fourth and fifth columns give the peak brightnesses (T_b) at 12 GHz and their separations (θ_{sep}) and position angles (P.A.) east of north between maser and reference sources. The sixth column gives the LSR velocities of the masers. The last column gives the FWHM size of the Gaussian restoring beam. Calibrators J1855+0251 (Fomalont et al. 2003) and J1907+0127 (Petrov et al. 2005) are from the VLBA Calibrator Survey, the other calibrators are from Xu et al. (2006b).

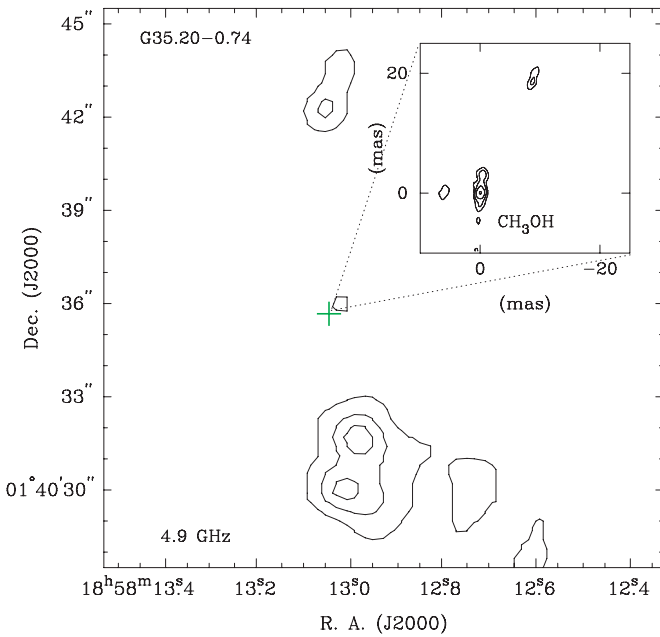


Figure 1. Images of 4.9 GHz radio continuum emission associated with the star-forming region G35.20–0.74, generated from archival VLA data (program AH241), and the velocity-integrated maser emission (inset). The position of the methanol masers is designated with a plus (+) sign. Contour levels are linearly spaced at 0.45 mJy for the continuum emission; they start at 0.06 Jy beam $^{-1}$ km s $^{-1}$ and increase by factors of 2 for the maser emission.

(A color version of this figure is available in the online journal.)

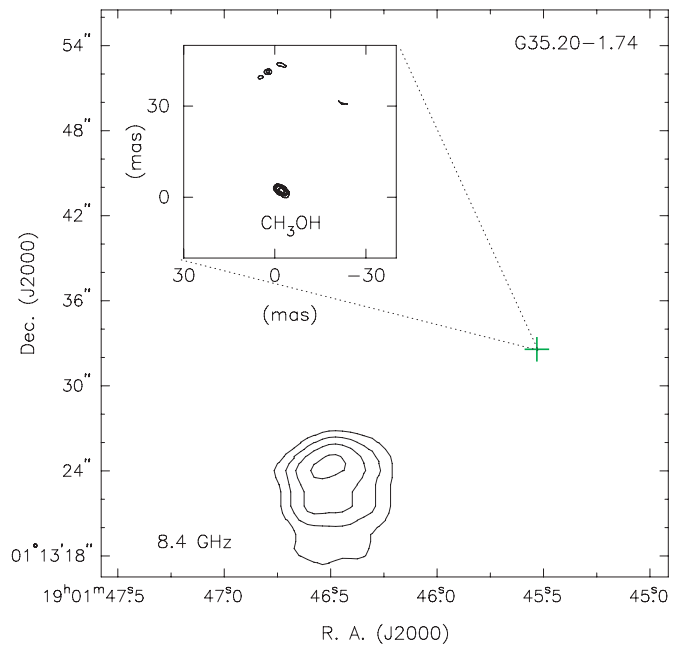


Figure 2. Images of 8.4 GHz radio continuum emission associated with the star-forming region G35.20–1.74, generated from archival VLA data (program AK477), and the velocity-integrated maser emission (inset). The position of the methanol masers are shown as a plus (+) sign. Contour levels start at 66 mJy beam $^{-1}$ and increase by factors of 2 for the continuum emission; they start at 0.27 Jy beam $^{-1}$ km s $^{-1}$ and increase by factors of 2 for the maser emission.

(A color version of this figure is available in the online journal.)

G35.20–1.74, respectively. The point-source response functions (dirty beams) had FWHMs of 1.9 by 0.8 mas at a P.A. of -8° east of north. After experimenting with different restoring beams, we adopted a circular restoring beam with a 1.2 mas FWHM for both maser sources and background sources. Figures 1 and 2 show radio continuum (from VLA archive data) and velocity-integrated methanol maser emission from these star-forming regions.

3. PARALLAX AND PROPER MOTION RESULTS

We fitted elliptical Gaussian brightness distributions to strong maser spots and the extragalactic radio sources for all four epochs. The change in position of each maser spot relative to each background radio source was modeled by the parallax sinusoid in both coordinates, determined by one parameter (the parallax), and a secular proper motion in each coordinate.

3.1. G35.20–0.74

Figure 3 shows maser reference channel images for G35.20–0.74 from the first and last epochs. Imaging sources near zero declination is generally problematic for radio interferometers, and we suspect that the low-level symmetric structures seen in the G35.20–0.74 images are caused by small calibration errors. However, since the parallax measurement comes almost exclusively from the east–west data, this should not be significant problem. Keeping this in mind, one can see that the emission appears dominated by a single compact component, and there is no significant variation over the 1.5 year time span of our observations. One of the three background sources (J1855+0215) proved to be very weak, and we used only J1855+0251 and J1907+0127 in the parallax fits. Figure 4 provides the images of background radio sources used for the fitting of parallax and proper motion for G35.20–0.74.

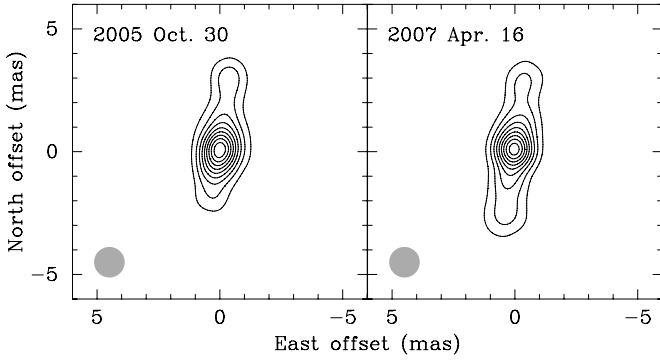


Figure 3. Images of reference maser source at $V_{\text{LSR}} = 28.3 \text{ km s}^{-1}$ in G35.20–0.74 at the first and last epoch. Observation dates are indicated in the upper left corner of each panel. The restoring beam is in the lower left corner. Contour levels are spaced linearly at 90 mJy beam^{-1} .

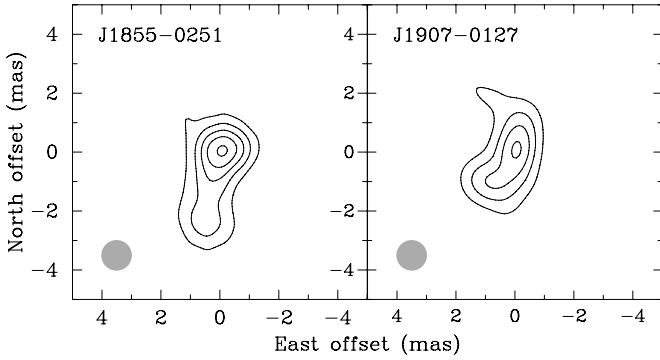


Figure 4. Images of extragalactic radio sources used for the parallax measurements of G35.20–0.74 from the first epoch observation on 2005 October 30. Source names are in the upper left corner of each panel. Contour levels are spaced linearly at $7.0 \text{ mJy beam}^{-1}$ for J1855+0251 and $10.0 \text{ mJy beam}^{-1}$ for J1907+0127.

Table 2
G35.20–0.74 Parallax and Proper Motion Fits

Maser V_{LSR} (km s^{-1})	Background Source	Parallax (mas)	μ_x (mas yr^{-1})	μ_y (mas yr^{-1})
27.9	J1855 + 0251	0.411 ± 0.057	-0.07 ± 0.10	-4.50 ± 0.33
27.9	J1907 + 0127	0.426 ± 0.037	-0.05 ± 0.06	-4.47 ± 0.10
27.5	J1855 + 0251	0.506 ± 0.083	-0.37 ± 0.14	-2.83 ± 0.27
27.5	J1907 + 0127	0.522 ± 0.094	-0.35 ± 0.16	-2.80 ± 0.25
27.9	Combined	0.456 ± 0.045	-0.07 ± 0.08	-4.47 ± 0.16
27.5			-0.29 ± 0.08	-2.79 ± 0.16

Notes. Combined fit used a single parallax parameter for both maser spots relative to the background sources, but a different proper motion was allowed for the two maser spots to allow for internal maser motions. Uncertainties are formal errors adjusted to give χ^2 per degree of freedom of unity, except for the “combined” parallax uncertainty which has been increased to allow for the difference between the parallaxes of the two maser spots.

In order to measure the parallax and proper motion of G35.20–0.74, we fitted the two brightest maser spots, at $V_{\text{LSR}} = 27.9$ and 27.5 km s^{-1} , and the two background radio sources, J1855+0251 and J1907+0127, for all four epochs. In Figure 5, we plot the positions of these two maser spots relative to the two background radio sources, with superposed curves representing the model maser tracks across the sky. The fitting results, listed in Table 2, reveal that the individually measured parallaxes and proper motions for two maser spots in G35.20–0.74 are somewhat different. However, the results using the two background sources are reasonably consistent. This suggests

that time variable maser structure in one or both spots, and not atmospheric calibration, may limit the parallax accuracy. Thus, we have increased the parallax uncertainty for the “combined” solution to half the average difference between the fits for the two maser spots. The combined parallax of the two astrometric maser spots is $0.456 \pm 0.045 \text{ mas}$, corresponding to a distance of $2.19^{+0.24}_{-0.20} \text{ kpc}$.

The average proper motion of the two maser spots is $-0.18 \pm 0.06 \text{ mas yr}^{-1}$ toward the east and $-3.63 \pm 0.11 \text{ mas yr}^{-1}$ toward the North. The difference in the northward proper motions of the two maser spots of $\pm 1.7 \text{ mas yr}^{-1}$ ($\pm 18 \text{ km s}^{-1}$) is unusually large compared to other sources given in Papers I–V (Reid et al. 2009a; Moscadelli et al. 2009; Xu et al. 2009; this paper; Brunthaler et al. 2009). While such an internal motion is not impossible, we suspect that the difference may be a result of the poor north–south beam of the interferometer for this near zero Declination source. At the distance implied by the parallax measurement, the average proper motions correspond to -1.9 km s^{-1} and -37.7 km s^{-1} eastward and northward, respectively. Completing the three-dimensional space velocity, the average LSR velocity of the spots is 27.7 km s^{-1} , which corresponds to a heliocentric radial velocity of 10.7 km s^{-1} .

3.2. G35.20–1.74

Figure 6 displays images of the maser reference channel for G35.20–1.74 from the first and last epoch. The emission appears dominated by a single compact component, and there is no significant variation over the 1.5 years spanned by our observations. In Figure 7, we show images of the four background radio sources at the first epoch. We fitted two-dimensional Gaussian brightness distributions to the four background radio sources and the two brightest maser spots at $V_{\text{LSR}} = 41.9 \text{ km s}^{-1}$ and 41.5 km s^{-1} . In Figure 8, we plot the positions of these maser spots relative to the two background radio sources with superposed curves representing the model maser tracks across the sky.

Our parallax estimates, given in Table 3, for three of the four background sources are consistent for an individual maser spot. The parallax estimate using J1903+0145 differs from the others by about 2σ , but gives the smallest post-fit residuals. Given the limited number of degrees of freedom for the fits, it is unclear whether the data for this background source is worse than for the other three background sources and has a fortuitously good fit, or if it is the best data and the data for the other three sources agree fortuitously well. Rather than make this decision, we use the data from all four background sources.

The difference in parallax between the two maser spots is roughly 0.10 mas . The scatter among the four measures for each spot suggests an uncertainty of about 0.03 mas , the joint error in the difference would be about 0.04 mas . So the discrepancy is just over 2σ . Changes in maser structure might be a possible cause. The 41.9 and 41.5 km s^{-1} masers varied by 3 and 6 Jy over the four epochs. However, with our limited data we cannot really evaluate which maser gives a better parallax. So we have used both and conservatively expanded the parallax uncertainty to half the difference between the individual values.

We adopt the “combined” parallax solution, which uses both maser spots and the four background sources, which gives a parallax for G35.20–1.74 of $0.306 \pm 0.045 \text{ mas}$. As done for source G35.20–0.74, we do not use the formal parallax uncertainty of $\pm 0.015 \text{ mas}$, but instead conservatively adopt a parallax uncertainty of $\pm 0.045 \text{ mas}$, which allows for the larger than expected difference in parallax estimates from the two

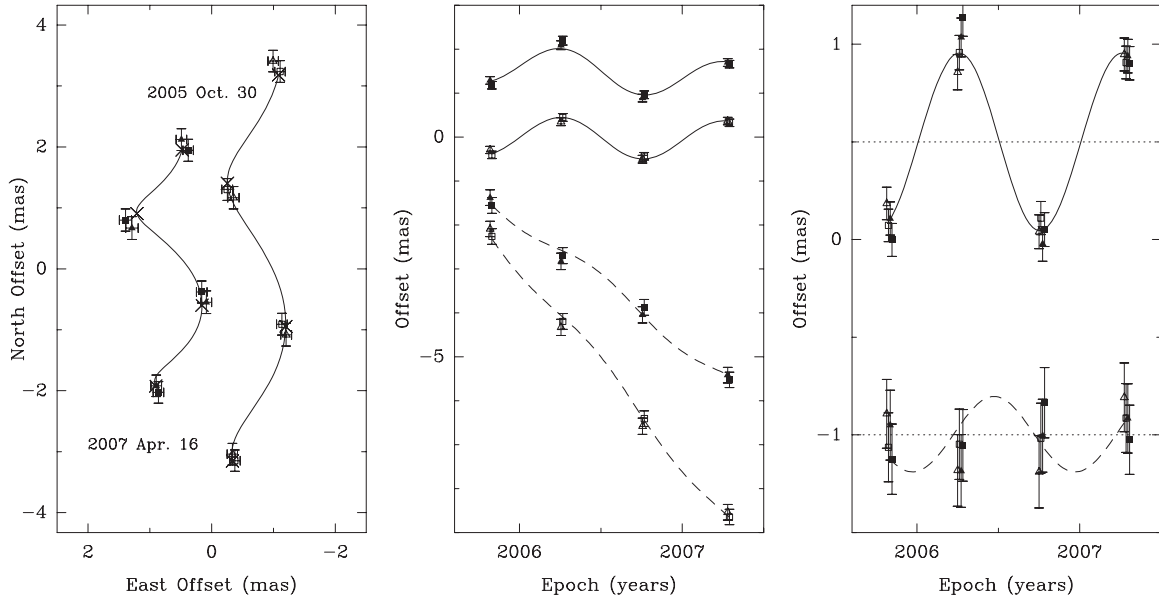


Figure 5. Parallax and proper motion data and best-fitting models for G35.20–0.74. Filled and opened markers are for maser spots at V_{LSR} of 27.9 km s^{-1} and 27.5 km s^{-1} , respectively. Plotted are positions of both maser spots relative to the two extragalactic radio sources: J1855+0251 (triangles) and J1907+0127 (squares). Left panel: positions with superposed curves representing the modeled maser track on the sky with the first and last epochs labeled. The expected positions from the parallax and proper motion fit are indicated (crosses). Middle panel: eastward (solid lines) and northward (dashed lines) offsets and best-fitting models versus time. Data for the eastward and northward positions are offset vertically and small time shifts have been added to the data for clarity. Right panel: same as the middle panel, except the best-fitting proper motions have been removed, allowing all data to be overlaid and the effects of only the parallax seen. The solid (dashed) line shows the combined fitted eastward (northward) parallax curve.

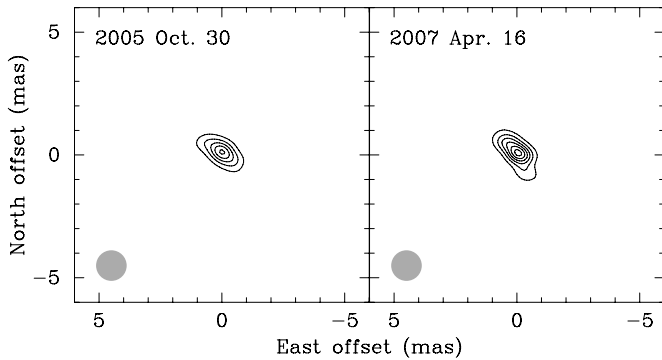


Figure 6. Images of reference maser source at $V_{\text{LSR}} = 41.5 \text{ km s}^{-1}$ in G35.20–1.74 at the first and last epochs. The epochs are indicated in the upper left corner of each panel. The restoring beam is in the lower left corner. Contour levels are spaced linearly at 1.2 and 1.5 Jy beam^{-1} , respectively.

maser spots. The parallax for G35.20–1.74 corresponds to a distance of $3.27^{+0.56}_{-0.42} \text{ kpc}$.

The proper motion estimates for the two maser spots and for all four background sources appear consistent within their joint uncertainties and the average proper motion is $-0.71 \pm 0.05 \text{ mas yr}^{-1}$ toward the east and $-3.61 \pm 0.17 \text{ mas yr}^{-1}$ toward the north. For the measured parallax, the proper motion corresponds to -11.0 km s^{-1} and -56.0 km s^{-1} eastward and northward, respectively. The average LSR velocity of the spots is 41.7 km s^{-1} , which corresponds to a heliocentric radial velocity of 24.8 km s^{-1} .

4. GALACTIC LOCATIONS AND THREE-DIMENSIONAL MOTIONS

In order to study the three-dimensional motion of the maser sources in the Galaxy, we convert their radial and proper motions from the equatorial heliocentric reference frame in which they

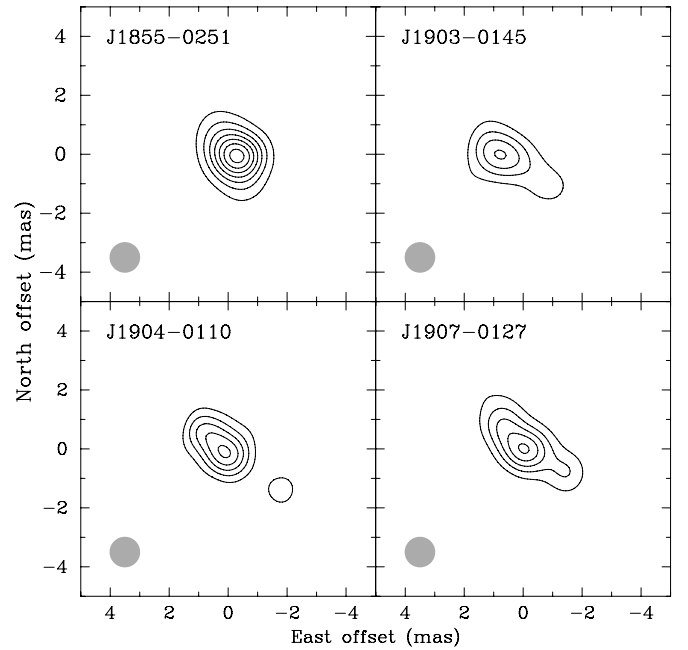


Figure 7. Images of background continuum sources used for the parallax measurements of G35.20–1.74 at the first epoch. Source names are in the upper left corner and restoring beams are in the lower left corner of each panel. Contour levels are spaced linearly at increments of 8.5 mJy beam^{-1} for J1855+0251, 9.5 mJy beam^{-1} for J1903+0145, and 15 mJy beam^{-1} for J1904+0110 and J1907+0127.

are measured into a Galactic reference frame. A convenient frame is one rotating with a constant speed at the position of the maser source: i.e., a “local standard of rest” for the location of maser. The methods used to convert to this frame will be documented in Reid (2009b, Paper VI). We use the IAU recommended values of $R_0 = 8.5 \text{ kpc}$ and $\Theta_0 = 220 \text{ km s}^{-1}$,

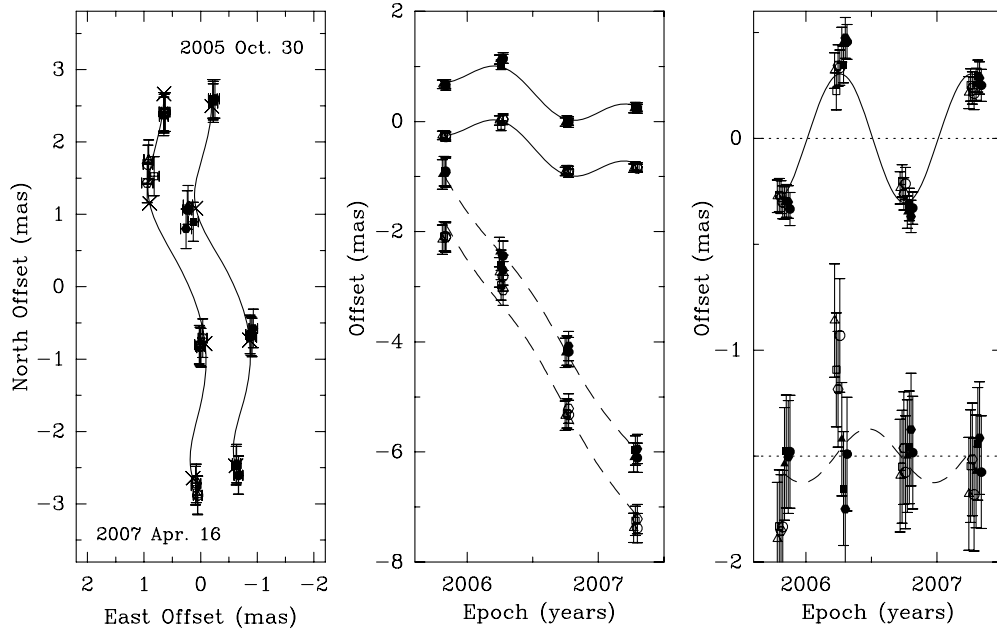


Figure 8. Parallax and proper motion data and fits for G35.20–1.74. Filled and opened markers are for maser spot at V_{LSR} of 41.9 km s^{-1} and 41.5 km s^{-1} , respectively. Plotted are position measurements of both maser spots relative to the four background sources: J1855+0251 (circles), J1903+0145 (triangles), J1904+0110 (squares), J1907+0127 (hexagons). Left panel: positions on the sky with the first and last epochs labeled. Data for the maser spot are offset horizontally for clarity. The expected positions from the parallax and proper motion fit are indicated (crosses). Middle panel: eastward (solid lines) and northward (dashed lines) positions and best fitting models versus time. Data for the eastward and northward positions are offset vertically and small time shifts have been added to the data for clarity. Right panel: same as the middle panel, except the best fit proper motions have been removed, allowing all data to be overlaid and the effects of only the parallax seen. The solid (dashed) line shows the combined fitted eastward (northward) parallax curve.

Table 3
G35.20–1.74 Parallax and Proper Motion Fits

Maser V_{LSR} (km s^{-1})	Background Source	Parallax (mas)	μ_x (mas yr^{-1})	μ_y (mas yr^{-1})
41.9	J1855 + 0251	0.272 ± 0.048	-0.76 ± 0.08	-3.83 ± 0.66
41.9	J1903 + 0145	0.220 ± 0.021	-0.67 ± 0.04	-3.71 ± 0.44
41.9	J1904 + 0110	0.287 ± 0.042	-0.76 ± 0.07	-3.66 ± 0.36
41.9	J1907 + 0127	0.274 ± 0.067	-0.75 ± 0.12	-3.85 ± 0.58
41.5	J1855 + 0251	0.368 ± 0.047	-0.78 ± 0.08	-3.62 ± 0.08
41.5	J1903 + 0145	0.319 ± 0.021	-0.70 ± 0.03	-3.50 ± 0.21
41.5	J1904 + 0110	0.385 ± 0.043	-0.78 ± 0.07	-3.44 ± 0.31
41.5	J1907 + 0127	0.363 ± 0.066	-0.76 ± 0.12	-3.63 ± 0.11
41.9	Combined	0.306 ± 0.045	-0.74 ± 0.07	-3.73 ± 0.24
41.5			-0.69 ± 0.07	-3.50 ± 0.24

Note. See Table 2 note.

and the Hipparcos solar motion values $U = 10.0 \pm 0.40$, $V = 5.2 \pm 0.60$, and $W = 7.2 \pm 0.40 \text{ km s}^{-1}$ (Dehnen & Binney 1998). For this Galactic model, G35.20–0.74 has a peculiar motion of -13 km s^{-1} in the direction of Galactic rotation, 0 km s^{-1} toward the Galactic Center and -8 km s^{-1} toward the North Galactic Pole. For G35.20–1.74, we find peculiar motion component of -16 km s^{-1} in the direction of Galactic rotation, 1 km s^{-1} toward the Galactic Center and -9 km s^{-1} toward the North Galactic Pole. Thus, both sources are rotating slower than the Galaxy spins, that is, slower than for a circular orbit for a flat rotation curve for the Galaxy. Neither source has a significant peculiar velocity component toward the Galactic center and both are moving toward the NGP at about -8 km s^{-1} .

Research on the structure of the Galaxy in Nanjing University is supported by the National Science Foundation of

China (NSFC) under grants 1062130, 10673024, 10703010 and 10733030, and NBRPC (973 Program) under grant 2007CB815403. Andreas Brunthaler was supported by the DFG Priority Programme 1177.

REFERENCES

- Braz, M. A., & Epchtein, N. 1983, *A&AS*, **54**, 167
 Brunthaler, A., et al. 2009, *ApJ*, **693**, 424 (Paper V)
 Caswell, J. L., & Haynes, R. F. 1983, *Aust. J. Phys.*, **36**, 417
 Caswell, J. L., Vaile, R. A., Ellingsen, S. P., Whiteoak, J. B., & Norris, R. P. 1995, *MNRAS*, **272**, 96
 Churchwell, E., Walmsley, C. M., & Cesaroni, R. 1990, 159, *A&AS*, **83**, 119
 De Buizer, J. M., Radomski, J. T., Telesco, C. M., & Pinal, R. K. 2004, *A&AS*, **36**, 1619
 De Buizer, J. M., & James, M. 2006, *ApJ*, **642L**, 57
 Dehnen, W., & Binney, J. J. 1998, *MNRAS*, **298**, 387
 Fomalont, E., Petrov, L., McMillan, D. S., Gordon, D., & Ma, C. 2003, *AJ*, **126**, 2562
 Forster, J. R., & Caswell, J. L. 1989, *A&A*, **213**, 339
 Genzel, R., & Downes, D. 1977, *A&AS*, **30**, 145
 Gibb, A. G., Hoare, M. G., Little, L. T., & Wright, M. C. H. 2003, *MNRAS*, **339**, 1011
 Hachisuka, K., et al. 2006, *ApJ*, **645**, 337
 Kalenskii, S. V., Promislov, V. G., Alakoz, A., Winnberg, A. V., & Johansson, L. E. B. 2000, *A&A*, **354**, 1036
 Ma, C., et al. 1998, *AJ*, **116**, 516
 Moscadelli, L., et al. 2009, *ApJ*, **693**, 406 (Paper II)
 Palagi, F., Cesaroni, R., Comoretto, G., Felli, M., & Natale, V. 1993, *A&AS*, **101**, 153
 Petrov, L., Kovalev, Yu. Y., Fomalont, E., & Gordon, D. 2005, *AJ*, **129**, 1163
 Reid, M. J., et al. 2009a, *ApJ*, **693**, 397 (Paper I)
 Reid, M. J., et al. 2009b, *ApJ*, submitted (Paper VI)
 Solomon, P. M., Rivolo, A. R., Barrett, J., & Yahil, A. 1987, *ApJ*, **319**, 730
 Vallee, J. P., & MacLeod, J. M. 1990, *ApJ*, **358**, 183
 Xu, Y., Reid, M. J., Zheng, X. W., & Menten, K. M. 2006a, *Science*, **311**, 54
 Xu, Y., Reid, M. J., Menten, K. M., & Zheng, X. W. 2006b, *ApJS*, **166**, 526
 Xu, Y., et al. 2009, *ApJ*, **693**, 413 (Paper III)